



## Clustering properties of g-selected galaxies at $z$ similar to 0.8

Ginevra Favole, Johan Comparat, Francisco Prada, Gustavo Yepes, Eric Jullo, Anna Niemic, Jean-Paul Kneib, Sergio A. Rodriguez-Torres, Anatoly Klypin, Ramin A. Skibba, et al.

### ► To cite this version:

Ginevra Favole, Johan Comparat, Francisco Prada, Gustavo Yepes, Eric Jullo, et al.. Clustering properties of g-selected galaxies at  $z$  similar to 0.8. *Monthly Notices of the Royal Astronomical Society*, 2016, 461 (4), pp.3421–3431. <10.1093/mnras/stw1483>. <hal-01440738>

**HAL Id: hal-01440738**

**<https://hal.science/hal-01440738v1>**

Submitted on 9 Sep 2021

**HAL** is a multi-disciplinary open access archive for the deposit and dissemination of scientific research documents, whether they are published or not. The documents may come from teaching and research institutions in France or abroad, or from public or private research centers.

L'archive ouverte pluridisciplinaire **HAL**, est destinée au dépôt et à la diffusion de documents scientifiques de niveau recherche, publiés ou non, émanant des établissements d'enseignement et de recherche français ou étrangers, des laboratoires publics ou privés.



Distributed under a Creative Commons CC BY 4.0 - Attribution - International License

# Clustering properties of $g$ -selected galaxies at $z \sim 0.8$

Ginevra Favole,<sup>1,2★</sup> Johan Comparat,<sup>1,2,3★†</sup> Francisco Prada,<sup>1,2,4,5</sup> Gustavo Yepes,<sup>3</sup>  
Eric Jullo,<sup>6</sup> Anna Niemiec,<sup>6</sup> Jean-Paul Kneib,<sup>7,6</sup> Sergio A. Rodríguez-Torres,<sup>1,2,3‡</sup>  
Anatoly Klypin,<sup>8</sup> Ramin A. Skibba,<sup>9</sup> Cameron K. McBride,<sup>10</sup> Daniel J. Eisenstein,<sup>10</sup>  
David J. Schlegel,<sup>4</sup> Sebastián E. Nuza,<sup>11</sup> Chia-Hsun Chuang,<sup>1,2§</sup> Timothée Delubac,<sup>7</sup>  
Christophe Yèche<sup>12</sup> and Donald P. Schneider<sup>13,14</sup>

<sup>1</sup>*Instituto de Física Teórica (IFT) UAM/CSIC, Universidad Autónoma de Madrid, Cantoblanco, E-28049 Madrid, Spain*

<sup>2</sup>*Campus of International Excellence UAM/CSIC, Cantoblanco, E-28049 Madrid, Spain*

<sup>3</sup>*Departamento de Física Teórica M-8, Universidad Autónoma de Madrid, Cantoblanco, E-28049 Madrid, Spain*

<sup>4</sup>*Lawrence Berkeley National Laboratory, 1 Cyclotron Road, Berkeley, CA 94720, USA*

<sup>5</sup>*Instituto de Astrofísica de Andalucía (CSIC), Granada E-18008, Spain*

<sup>6</sup>*Laboratoire d'Astrophysique de Marseille – LAM, Université d'Aix-Marseille and CNRS, UMR7326, F-13388 Marseille, France*

<sup>7</sup>*Laboratoire d'Astrophysique, Ecole Polytechnique Fédérale de Lausanne (EPFL), Observatoire de Sauverny, CH-1290 Versoix, Switzerland*

<sup>8</sup>*Astronomy Department, New Mexico State University, MSC 4500, PO Box 30001, Las Cruces, NM 88003-8001, USA*

<sup>9</sup>*Center for Astrophysics and Space Sciences, University of California, 9500 Gilman Drive, San Diego, CA 92093, USA*

<sup>10</sup>*Harvard-Smithsonian Center for Astrophysics, 60 Garden Street, Cambridge, MA 02138, USA*

<sup>11</sup>*Leibniz-Institut für Astrophysik Potsdam (AIP), An der Sternwarte 16, D-14482 Potsdam, Germany*

<sup>12</sup>*CEA, Centre de Saclay, IRFU, F-91191 Gif-sur-Yvette, France*

<sup>13</sup>*Department of Astronomy and Astrophysics, The Pennsylvania State University, University Park, PA 16802, USA*

<sup>14</sup>*Institute for Gravitation and the Cosmos, The Pennsylvania State University, University Park, PA 16802, USA*

Accepted 2016 June 17. Received 2016 June 17; in original form 2015 July 15

## ABSTRACT

Current and future large redshift surveys, as the Sloan Digital Sky Survey IV extended Baryon Oscillation Spectroscopic Survey (SDSS-IV/eBOSS) or the Dark Energy Spectroscopic Instrument (DESI), will use emission-line galaxies (ELGs) to probe cosmological models by mapping the large-scale structure of the Universe in the redshift range  $0.6 < z < 1.7$ . With current data, we explore the halo–galaxy connection by measuring three clustering properties of  $g$ -selected ELGs as matter tracers in the redshift range  $0.6 < z < 1$ : (i) the redshift-space two-point correlation function using spectroscopic redshifts from the BOSS ELG sample and VIPERS; (ii) the angular two-point correlation function on the footprint of the CFHT-LS; (iii) the galaxy–galaxy lensing signal around the ELGs using the CFHTLenS. We interpret these observations by mapping them on to the latest high-resolution MultiDark Planck  $N$ -body simulation, using a novel (Sub)Halo-Abundance Matching technique that accounts for the ELG incompleteness. ELGs at  $z \sim 0.8$  live in haloes of  $(1 \pm 0.5) \times 10^{12} h^{-1} M_{\odot}$  and  $22.5 \pm 2.5$  per cent of them are satellites belonging to a larger halo. The halo occupation distribution of ELGs indicates that we are sampling the galaxies in which stars form in the most efficient way, according to their stellar-to-halo mass ratio.

**Key words:** galaxies: distances and redshifts – galaxies: haloes – galaxies: statistics – cosmology: observations – cosmology: theory – large-scale structure of Universe.

## 1 INTRODUCTION

By investigating the properties of galaxy clustering within the cosmic web, it is possible to constrain cosmology and infer the growth of structure and the expansion history of the Universe (Weinberg et al. 2013). In fact, galaxy clustering measurements using last-generation large-volume redshift surveys, as the Sloan Digital Sky Survey (SDSS; York et al. 2000; Gunn et al. 2006; Smee et al.

\* E-mail: g.favole@csic.es (GF); johan.comparat@uam.es (JC)

† Severo Ochoa IFT Fellow.

‡ Campus de Excelencia Internacional UAM/CSIC Scholar.

§ MultiDark Fellow.

2013) and the SDSS-III Baryon Oscillation Spectroscopic Survey (BOSS; Eisenstein et al. 2011; Dawson et al. 2013) provide robust information about both the evolution of galaxies and the cosmological framework in which these complex structures live. In order to interpret such measurements, we need to understand the relation between the theory-predicted dark matter field and its luminous counterpart i.e. the discrete galaxy map (Cooray & Sheth 2002).

Luminous low-redshift galaxies have already been connected to their dark matter haloes in a precise manner, through weak lensing and clustering analysis as a function of galaxy luminosity and stellar mass. Baldry et al. (2004), Zehavi et al. (2011) and Guo et al. (2015) measured the clustering properties of the SDSS ‘blue cloud’ and ‘red sequence’ in the local Universe (SDSS median redshift  $z \sim 0.1$ ; Abazajian et al. 2009), as a function of magnitude and colour. Their results show that at a given luminosity, the blue sample has a lower clustering amplitude and a smaller correlation length compared to the red one.

Guo et al. (2014) investigated the clustering luminosity and colour dependence of BOSS CMASS DR10 (Anderson et al. 2014), and found that more luminous galaxies are more clustered and hosted by more massive haloes. For luminous red galaxies (LRGs), these masses are  $\sim 10^{13} - 10^{14} h^{-1} M_{\odot}$ , at fixed luminosity, progressively redder galaxies are more strongly clustered on small scales, which can be explained by having a larger fraction of these galaxies in the form of satellites in massive haloes. Favole et al. (2015) measured galaxy clustering in the BOSS CMASS DR11 (Anderson et al. 2014) sample at  $z > 0.55$  as a function of colour, and proposed a new statistic to extract robust information about small-scale redshift-space distortions and large-scale galaxy bias. Consistent with many previous results (e.g. Zehavi et al. 2005; Wang et al. 2007; Swanson et al. 2008), they found that, compared to the blue population, red galaxies reside in more massive haloes, show a higher clustering amplitude, large-scale bias and peculiar velocities.

This type of clustering analysis has recently been extended to higher redshifts thanks to the VIMOS Public Extragalactic Survey (VIPERS; Guzzo et al. 2014; Garilli et al. 2014) and DEEP2 survey (Newman et al. 2013). Compared to DEEP2, VIPERS has a much larger volume but has a lower redshift limit however, the signal-to-noise ratio in its spectroscopic measurements is higher. Using VIPERS data, Marulli et al. (2013) measured the clustering properties of galaxies at redshift  $z = 0.8$  as a function of their luminosity and stellar mass, and found that the clustering amplitude and the correlation length increase with these two quantities; see also the PRISM Multi-object Survey (PRIMUS) results by Skibba et al. (2015) and Bray et al. (2015). Mostek et al. (2013) measured the clustering of the red sequence and the blue cloud at  $z = 0.9$ , as a function of their stellar mass and star formation history, using DEEP2 data. They argued that blue galaxies are more clustered in the local Universe than at  $z = 0.9$ , and red galaxies are much more clustered locally than at high redshift. They also suggested that the clustering trend observed with star formation rate (SFR) can be explained mostly by the correlation between stellar mass and clustering amplitude for blue galaxies. Coil et al. (2008) studied the DEEP2 clustering dependence on colour and luminosity, and found that the dependence on colour is much stronger than with luminosity, and is as strong with colour at  $z \sim 1$  as locally. They claimed no dependence of the clustering amplitude on colour for galaxies in the red sequence, but a significant dependence for galaxies within the blue cloud. Cooper et al. (2008) investigated the connection between star formation (SF) and environment in DEEP2 data at  $z \sim 0.1$ , and  $z \sim 1$ . Their results indicate that, locally, galaxies in regions of higher overdensity have lower SFRs, and their stars form

more slowly than in their counterparts in lower density regions. At  $z \sim 1$ , this SFR–overdensity relation is inverted; this is in part due to a population of bright, blue galaxies in dense environments, which lacks a counterpart in the local Universe, and is thought to evolve into members of the red sequence from redshift 1 to 0.

The combination of clustering with weak galaxy–galaxy lensing (see e.g. Bartelmann 1999) allows one to gain insight on the large-scale structure formation, and directly probe the stellar-to-halo mass relation (SHMR; Leauthaud et al. 2011). The galaxy–halo connection has been measured at  $z < 1$  by Leauthaud et al. (2012), Shan et al. (2015), and Coupon et al. (2015), using three different weak lensing surveys [COSMOS: Scoville et al. (2007); CFHT-Stripe82 and CFHTLenS;<sup>1</sup> Heymans et al. (2012); Erben et al. (2013)]; all obtained consistent results. Leauthaud et al. (2012) performed the first joint analysis of galaxy–galaxy weak lensing, galaxy clustering, and galaxy number densities using COSMOS data, and provided robust constraints on the shape and redshift evolution of the (Sub)Halo-Abundance Matching (SHAM) relation in the redshift range  $0.2 < z < 1$ . At low stellar mass, the halo mass scales proportionally to  $M_{*}^{0.46}$ ; this scaling does not evolve significantly with redshift. At  $M_{*} > 5 \times 10^{10} M_{\odot}$ , the SHMR rises sharply, causing the stellar mass of a central galaxy to become a poor tracer of its parent halo mass. Combining observations in the CFHT-LenS/VIPERS field from the near-UV to the near-IR, Coupon et al. (2015) found that the SHMR for the central galaxies peaks at  $M_{h,peak} = (1.9^{+0.2}_{-0.1} \times 10^{12} M_{\odot})$ , and its amplitude decreases as the halo mass increases. Hearin et al. (2014) presented new measurements of the galaxy two-point correlation function and the galaxy–galaxy lensing signal from SDSS, as a function of colour and stellar mass, and demonstrated that the age-matching model (Hearin & Watson 2013), which states that older haloes tend to host galaxies with older stellar populations, exhibits remarkable agreement with these and other statistics of low-redshift galaxies.

Current SHAM (Conroy, Wechsler & Kravtsov 2006; Trujillo-Gomez et al. 2011; Klypin et al. 2013; Nuza et al. 2013) and halo occupation distribution (HOD; Berlind & Weinberg 2002; Kravtsov et al. 2004; Zheng et al. 2005; Zheng, Coil & Zehavi 2007) models correctly reproduce the clustering measurement mentioned above. SHAM maps observed galaxies on to dark matter haloes directly from  $N$ -body cosmological simulations, according to a precise monotonic correspondence between halo and galaxy number densities. The HOD method is an analytical prescription to populate simulated haloes with galaxies, in which the assignment is performed by interpolating the HOD at the values of the desired halo masses. In this sense, the SHAM approach returns a model which is built directly on the considered simulation box.

Next generation high-redshift surveys as SDSS-IV/eBOSS (Dawson et al. 2016), Subaru Prime Focus Spectrograph (Sugai et al. 2012; Smee et al. 2014), DESI (Schlegel et al. 2015), 4MOST<sup>2</sup> and Euclid<sup>3</sup> (Laureijs et al. 2011; Sartoris et al. 2016) will use emission-line galaxies (ELGs) as BAO tracers to explore the Universe large-scale structure out to  $z \sim 2$ . Observing ELGs, learning how to model their clustering properties and understanding how they populate their host haloes are therefore crucial points that we need to understand in order to select the targets for future experiments. From the observational point of view, the recent increment of available ELG spectroscopic data (Guzzo et al. 2014; Comparat

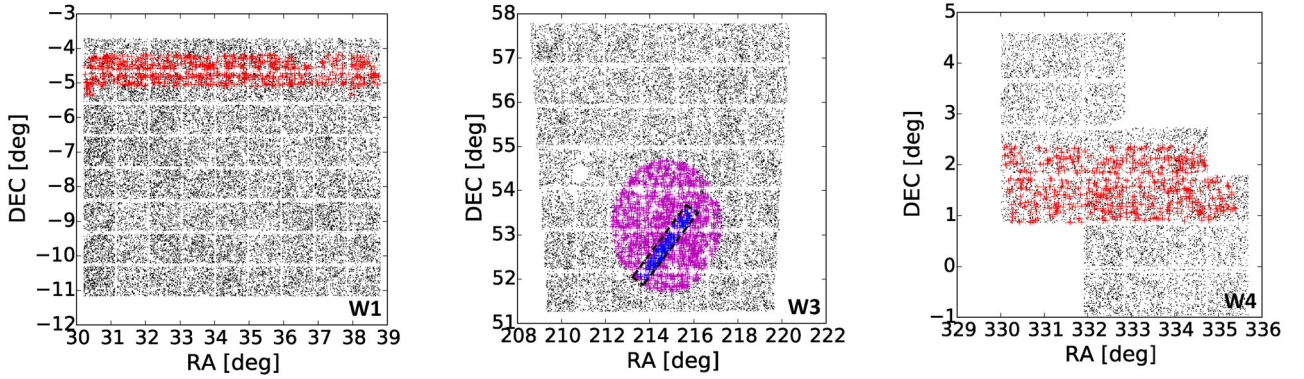
<sup>1</sup> <http://www.cfht.hawaii.edu/Science/CFHTLS/>

<sup>2</sup> <https://www.4most.eu/cms/>

<sup>3</sup> <http://sci.esa.int/euclid/>

**Table 1.** ELG photometric data per CFHT-LS Wide field after applying the bright star and bad field mask.

Field	W1	W3	W4	All
centre $\alpha, \delta$	$35^\circ, -7^\circ$	$215^\circ, 54^\circ$	$333^\circ, 2^\circ$	–
area (deg <sup>2</sup> )	63.75	44.22	23.3	131.27
$N$	32 808	22 195	11 025	66 028
$N$ (deg <sup>-2</sup> )	514.64	501.92	473.18	502.99
$z_{\text{phot}}$ quartiles	0.78 / 0.88 / 1.03	0.77 / 0.88 / 1.05	0.78 / 0.88 / 1.03	0.78 / 0.88 / 1.03
$z_{\text{phot}}$ deciles D10, D90	0.7 / 1.24	0.68 / 1.29	0.69 / 1.25	0.69 / 1.26
$N$ ( $0.6 < z_{\text{phot}} < 1$ )	23 433	15 242	7861	46 536
$N$ ( $0.6 < z_{\text{phot}} < 1$ ) (deg <sup>-2</sup> )	367.58	344.69	337.38	354.51
$z_{\text{phot}}$ quartiles	0.75 / 0.83 / 0.9	0.74 / 0.81 / 0.89	0.75 / 0.83 / 0.89	0.75 / 0.82 / 0.89

**Figure 1.** Photometric (black points) and spectroscopic (VIPERS: red crosses in the right- and left-hand panels; BOSS: magenta crosses forming the oval in the central panel; DEEP2: blue crosses in the dashed box in the central panel) coordinates of our ELG sample in the three CFHT-LS Wide fields.

et al. 2015) allows one to measure their clustering properties over about  $12 \text{ deg}^2$  at  $z = 0.8$  (corresponding to a comoving volume of  $V \sim 10.6 \times 10^6 h^{-3} \text{ Mpc}^3$  in the Planck cosmology; see Section 3 for details), which represents a dramatic improvement.

Comparat et al. (2013) demonstrated that neither a standard HOD nor a traditional SHAM technique are able to reproduce the angular clustering of ELGs on small scales. In fact, both techniques are based on the assumption that the galaxy sample to model is complete, but this is not the case of the ELGs, which are highly incomplete in stellar mass. One could instead use semi-analytic models (SAMs) of galaxy formation and hydrodynamic simulations, but they lack mass resolutions to model ELGs.

The aim of this work is to provide a modified version of the standard SHAM prescription, directly based on the latest MultiDark  $N$ -body simulation with Planck cosmology, that accounts for the ELG incompleteness and returns suitable mock galaxy catalogues able to accurately predict the ELG angular and redshift-space clustering, respectively, on small and larger scales. These mock catalogues are released to the public.

The paper is organized as follows. Section 2 describes the data sets and the MultiDark simulation box used in our analysis. In Section 3 we present our ELG clustering and weak lensing measurements. In Section 4 we explain how we model the ELG clustering and we present our main results. Section 5 discusses the implications of our ELG clustering analysis in a galaxy evolution perspective, and Section 6 summarizes our main results.

Throughout the paper, we assume the Planck cosmology (Planck Collaboration XVI 2014) and magnitudes in the AB system (Oke & Gunn 1983).

## 2 DATA AND SIMULATION

### 2.1 Data sets

We build our ELG galaxy sample using the Canada-France-Hawaii Telescope Legacy Survey (CFHT-LS) Wide T0007<sup>4</sup> photometric redshift catalogue (Ilbert et al. 2006; Coupon et al. 2009). We apply a  $g$ -band magnitude cut,  $20 < g < 22.8$  (Fukugita et al. 1996), to select galaxies with bright emission lines and low dust at  $z < 1$ . We also apply a colour selection,  $-0.5 < (u - r) < 0.7(g - i) + 0.1$ , to remove the low-redshift galaxies. For details on the selection function, see Comparat et al. (2015). Then, to obtain the largest possible area, we convert the  $i$ -selection into the new Megacam  $i$ -band filter.<sup>5</sup> For the W1, W3 and W4<sup>6</sup> fields, we derive an average density of about 500 ELGs per deg<sup>2</sup>, 70 per cent of which have a photometric redshift in the range  $0.6 < z < 1$ . The densities of each field are reported in Table 1, and the errors on the photometric redshift are  $\sigma_z < 0.05(1 + z)$  for  $i < 22.5$  and  $z < 1$ . The  $ugri$  ELG selection is brighter than  $i < 22.5$ . The RA, DEC coordinates for the three fields are shown in Fig. 1.

We match the photometric targets to the available spectroscopic surveys – BOSS DR12, DEEP2, VIPERS (Bolton et al. 2012; Newman et al. 2013; Guzzo et al. 2014; Alam et al. 2015) – within 1 arcsec radius; see Table 2. Based on KS-tests, the VIPERS, BOSS and DEEP2 spectroscopic selections constitute fair sub-samples of

<sup>4</sup> <http://www.cfht.hawaii.edu/Science/CFHTLS/>

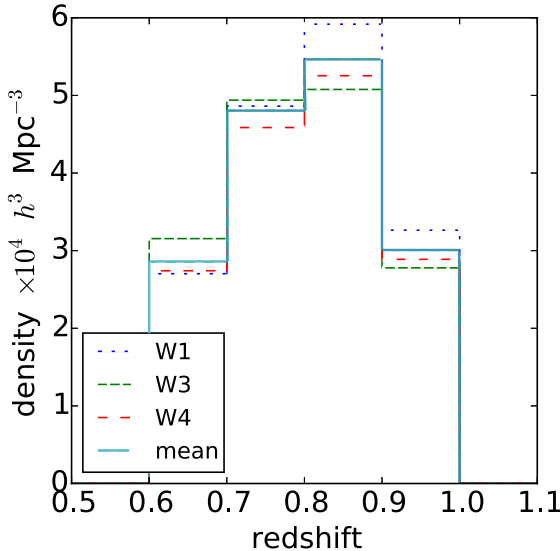
<sup>5</sup> <http://www4.cadc-ccda.hia-ihp.nrc-cnrc.gc.ca/en/megapipe/docs/filt.html>

<sup>6</sup> <http://www.cfht.hawaii.edu/Science/CFHTLS/T0007/T0007-docsu10.html>



**Table 2.** ELG spectroscopic data.

Survey	Match	Good $z$	$0.6 < z < 1$	area (deg <sup>2</sup> )	$\bar{z}$
VIPERS W1	1223	942	760	5.478	0.803
BOSS W3	2145	1876	1357	6.67	0.803
DEEP2 W3	225	222	156	0.5	0.803
VIPERS W4	1148	846	680	5.120	0.795
All	4741	3886	2953	17.668	0.803

**Figure 2.** ELG weighted spectroscopic redshift distribution per unit volume for the W1, W3, and W4 Wide fields (dashed and dotted histograms), and their mean value (solid line).

the complete selection: the hypothesis that they are drawn from the same distribution cannot be rejected at the 90 per cent confidence level. For these samples, we create random catalogues with the same redshift distribution of the data and 30 times denser. Fig. 2 displays the ELG spectroscopic redshift distribution per unit volume for the three Wide fields (dashed, dotted, dot–dashed histograms), and their mean (solid line). Two thirds of the galaxy density is located in the redshift range  $0.7 < z < 0.9$ , while both the intervals  $0.6 < z < 0.7$  and  $0.9 < z < 1$  contain one sixth of the sample. According to the ELG selection function in Comparat et al. (2015), we select only galaxies at  $z > 0.6$  since we are not interested in low-redshift objects. We have investigated further the impact of the higher redshift cut,  $z < 1$ , on the angular clustering by imposing to the ELG sample different redshift thresholds:  $z < 1, 1.2, 1.4, 1.6$ . In all these samples the lower redshift cut is fixed at  $z > 0.6$  and we have imposed the  $i < 22.5$  magnitude cut to eliminate bad photometric redshifts. We find that including ELGs at  $z \geq 1$ , we are slightly enhancing the galaxy number density of our sample and consequently suppressing the amplitude of  $w(\theta)$ , but we do not see any substantial change in the angular clustering trend with respect to the  $z < 1$  case. We therefore restrict the analysis to the redshift range  $0.6 < z < 1$ .

## 2.2 Multidark simulations

The MultiDark Planck simulation (MDPL, Klypin et al. 2014; [www.MultiDark.org](http://www.MultiDark.org)) contains  $3840^3$  particles in a  $1 h^{-1}$  Gpc box,

and was created adopting Planck  $\Lambda$  Cold Dark Matter ( $\Lambda$ CDM) cosmology (Planck Collaboration XVI 2014). Haloes are identified based on density peaks including substructures using the bound density maximum halo finder (Klypin & Holtzman 1997; Riebe et al. 2013).

We use the MDPL halo catalogues to build a mock light-cone that matches the mean ELG redshift distribution shown in Fig. 2. Given the high density of the ELG tracers and their expected low-mass host haloes, the MDPL box is an excellent compromise between numerical resolution and volume. We apply the SURVEY GENERATOR code (SUGAR; Rodríguez-Torres et al. 2016) to the 11 snapshots available from MDPL to construct a light-cone with a volume ten times the observations that covers the redshift range  $0.6 < z < 1$  ( $\sim 1 h^{-1}$  Gpc depth). The procedure used is analogous to the method presented by Blaizot et al. (2005) and Kitzbichler & White (2007), and can be summarized as follows:

(i) Set the properties of the light-cone: angular mask, radial selection function (number density) and number of snapshots within the redshift range considered. Each slice of the light-cone is constructed by selecting all haloes from every MDPL snapshot. The thickness of a slice at redshift  $z_i$  is given by  $[(z_i + z_{i-1})/2, (z_i + z_{i+1})/2]$ .

(ii) Place an observer (i.e.  $z = 0$ ) inside the box and shift the Cartesian coordinates of the box in such a way that the observer occupies the central point of the box at  $z = 0.8$ .

(iii) Convert from Cartesian  $(x, y, z)$  to spherical  $(\alpha, \delta, r_c)$  coordinates, where  $r_c$  is the comoving distance in real space. The redshift of each point will be:

$$r_c(z) = \int_a^b \frac{cdz'}{H_0 \sqrt{\Omega_m(1+z')^3 + \Omega_\Lambda}}. \quad (1)$$

(iv) From each snapshot, select the (sub)haloes so that  $(z_i + z_{i-1})/2 < z < (z_i + z_{i+1})/2$  and  $\alpha/\delta$  lie inside the sky window. Since the ELG observational data represent haloes with typical masses  $\sim 10^{12} h^{-1} M_\odot$ , in the light-cone we include all haloes for which the simulation is complete i.e.  $\log(M_h/h^{-1} M_\odot) > 11.2$ .

(v) Using the halo velocities,  $v_p$ , we compute the peculiar velocity contribution for each object along the line of sight and derive its distance in redshift-space as

$$s = r_c + (v_p \cdot r_c)/(aH(z)), \quad (2)$$

where  $a = (1+z)^{-1}$  is the scale factor and  $H(z)$  is the Hubble parameter at redshift  $z$ .

(vi) Finally, select objects from the light-cone using our selection function.

Throughout the paper we will designate our light-cone as ‘MDPL-LC’. Section 4 describes in detail the halo selection and the SHAM modelling adopted to determine the HOD of our ELG sample.

### 3 MEASUREMENTS

Using the ELG sample described in Section 2.1, we measure both galaxy clustering and galaxy–galaxy lensing. The following provides a detailed description of our measurements.

#### 3.1 Galaxy clustering

We estimate both the angular,  $w(\theta)$ , and the redshift-space,  $\xi(s)$  (hereafter  $\xi^s$ ), two-point correlation functions following the procedures described by Landy & Szalay (1993), Coupon et al. (2012) and de la Torre et al. (2013).

To compute  $\xi^s$  on the VIPERS and the BOSS ELG samples (see Table 2), independently, we create linear bins in separations of  $1 h^{-1}$  Mpc at  $s < 10 h^{-1}$  Mpc, and  $4 h^{-1}$  Mpc for  $10 < s < 40 h^{-1}$  Mpc. We then correct the impact of redshift errors and catastrophic redshifts to recover the correlation function down to  $1 h^{-1}$  Mpc. The ELG we are targeting are observed using three plates overlapping the same area of the sky. This configuration guarantees that all the targets are observed at the end of the process and there is no fibre collision (Blanton et al. 2003; Reid et al. 2014). We correct for the finite size of VIPERS following de la Torre et al. (2013), and define the survey completeness in terms of target sampling rate (TSR) and the spectroscopic success rates (SSR). The first quantity weights our ability of obtaining spectra from the potential targets meeting the survey selection in the parent photometric sample. For each galaxy in the spectroscopic catalogue, we count the number of objects that lie within a given radius in the spectroscopic ( $N_{\text{targeted}}$ ) and in the photometric ( $N_{\text{parent}}$ ) sample. The TSR is then given by the ratio  $TSR = N_{\text{targeted}}/N_{\text{parent}}$ . The SSR represents our ability of determining galaxy redshifts from observed spectra. To compute it, we replace the bad redshifts in the spectroscopic catalogue with good photometric redshifts. Galaxies with good spectra are assigned flag = 0 ( $N_{\text{good}}$ ); galaxies with replaced redshifts are assigned flag = 1 ( $N_{\text{targeted}}$ ). The SSR is then computed as the ratio  $SSR = N_{\text{good}}/N_{\text{targeted}}$ . The contribution of each galaxy in the clustering pair counts is then weighted by  $w = 1/(TSR \cdot SSR)$ . Finally, we combine the VIPERS and BOSS measurements weighted by the projected density of each field. The resulting redshift-space correlation function is displayed in the bottom panel of Fig. 3; by fitting a power-law model,  $\xi(s) = (s/s_0)^\alpha$ , in the separation range  $2 < s < 30 h^{-1}$  Mpc, we find  $s_0 = (5.3 \pm 0.2) h^{-1}$  Mpc and  $\alpha = -1.6 \pm 0.1$ .

Analogously, we calculate the angular 2PCF,  $w(\theta)$ , using photometric redshifts from the W1, W3 and W4 CFHT-LS fields. The points are corrected from the integral constraint following Tinker et al. (2010) and Coupon et al. (2012) to account for the restricted area of observation. On scales  $\theta < 0.05^\circ$ , all three fields provide consistent measurements. At larger scales, the clustering signals in the W1 and W4 fields do not decrease as rapidly as expected, probably pointing to possible systematics that need to be investigated further. We therefore use only the measurement on the W3 field, which appears the most robust (see Fig. 3, top panel). The  $w(\theta)$  of the W3 field is in perfect agreement with fig. 9 (panel 4) in Comparat et al. (2013). This result was computed on the Stripe 82 region (Stoughton et al. 2002), with three times larger area. At the mean redshift of the sample,  $z = 0.8$ , one degree corresponds to  $18.847 h^{-1}$  Mpc; thus,  $w(\theta)$  spans the range from  $\sim 40 h^{-1}$  kpc up to  $\sim 20 h^{-1}$  Mpc. We investigate further the impact on the clustering amplitude of including the tails of the photometric distribution, i.e.  $z_{\text{phot}} < 0.6$  and  $z_{\text{phot}} > 1$ . This inclusion does not produce any substantial change in  $w(\theta)$ , except for some additional noise. We

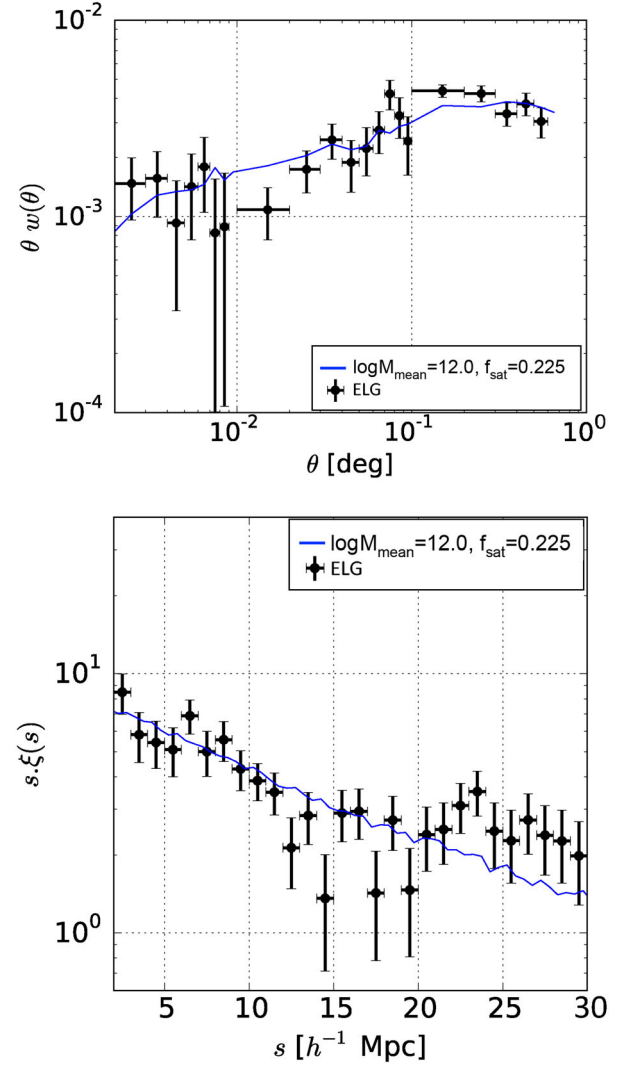


**Figure 3.** Two-point angular (top panel) and redshift-space (bottom panel) ELG correlation functions (points), together with our best-fitting model (blue line), which corresponds to the point highlighted by a star in Fig. 6.

also test how photometric uncertainties affect the clustering errors computed via mock resampling. To this purpose, following Coupon et al. (2012), we perturb our original redshift distribution by applying a photometric scatter with mean  $\sigma_z = 0.035(1 + z)$ . We then quantify the number of photometric objects that, due to this scatter, enter the ELG selection in the range  $0.6 < z < 1$  from the lower and higher tails of the distribution, and the objects that exit. We find that only 2.5 per cent photometric redshifts enter the ELG selection in the range  $0.6 < z < 1$  from the upper and lower tails, and their effect on the clustering is negligible.

To estimate the errors on our galaxy clustering measurements, since the simulated light-cone area is larger than the data ( $\sim 560 \text{ deg}^2$ ), we divide the best MDPL-LC model into independent (i.e. non-overlapping) realizations of our ELG data (8 for the photometric and 24 for the spectroscopic samples), and obtain sample variance diagonal errors that we use rather than Poisson errors. Including the photometric uncertainties in our jackknife resamplings does not provoke any significant change in the error estimates. We neglect a full-covariance analysis because the number

of sub-samples we have is too small to produce reliable covariance estimates. Including also the off-diagonal elements of the covariance matrices would result in large fluctuations of the error bars. Of course, excluding covariances we are adopting a simplified approach, but it provides a good sense of how the SDSS BOSS ELG clustering behaves. On the other hand, the ELG sample considered here is too sparse to derive tight constraints from our clustering analysis. New-generation large-volume spectroscopic surveys as eBOSS, DESI and 4MOST, will provide new data with unprecedented statistics, sky coverage and imaging quality. Using those data, a fully covariant approach will return reliable and accurate error estimates.

We compare the combined  $\xi^s$  measurement from BOSS and VIPERS to previous measurements by Marulli et al. (2013) to provide a first interpretation. Our result matches both the clustering signal of galaxies selected in the stellar mass range  $9.5 < \log(M_*/h^{-1} M_\odot) < 11$ , and the clustering of galaxies selected by absolute magnitude in the interval  $-22 < M_B - 5\log(h) < -20.5$ . Using the SHMR from Leauthaud et al. (2012), Shan et al. (2015) and Coupon et al. (2015), we can deduce a rough estimate of the halo masses populated by our ELG sample i.e.  $11.6 < \log(M_h/h^{-1} M_\odot) < 12.7$ . These halo masses are typical of Milky Way size haloes, being much less massive than those hosting the LRG sample, see Nuza et al. (2013).

In the angular clustering measurement, the change of slope occurs at  $\theta \sim 0.01^\circ$ , corresponding to  $\sim 200 h^{-1}$  kpc. Using MDPL, we derive the relation between halo mass and virial radius at  $z \sim 0.8$ ; haloes with virial radius  $\sim 200 h^{-1}$  kpc occupy the mass range  $M_h = (0.5 - 1) \times 10^{12} h^{-1} M_\odot$ . Since a single galaxy per halo would not induce such a change in the  $w(\theta)$  slope, this result implies a satellite fraction of approximately 22.5 per cent (see Section 4). Fig. 3 displays a good agreement between our clustering measurements and predictions for ELG haloes of mass  $10^{12} h^{-1} M_\odot$  with this satellite fraction.

### 3.2 Weak lensing

We use the latest weak lensing catalogues produced by the Canada-France-Hawaii Telescope Lensing Survey (CFHTLenS; Heymans et al. 2012; Erben et al. 2013) on the W1 and W3 fields to measure the galaxy–galaxy lensing around 47485 ELG lenses. This measurement allows one to constrain the halo masses. We follow Gillis et al. (2013) and apply only the multiplicative correction,  $m_s$ , to the shear measurement and avoid the  $c_2$  correction. We measure the tangential shear,  $\gamma'$ , around the photometric ELG sample as a function of the radial distance from the lenses using the (Vander, Kuijken & Schrabback 2011) estimator:

$$\Delta\Sigma = \left[ \frac{\sum_{ls} w_{ls} \gamma'_{ls} \Sigma_c}{\sum_{ls} w_{ls}} \right] / \left[ \frac{\sum_{ls} w_{ls} (1 + m_s)}{\sum_{ls} w_{ls}} \right], \quad (3)$$

where the sum runs over the lens–source pairs ( $ls$ ) and the  $w_{ls}$  values are the weight obtained by lensfit.

Since the lenses are at the higher tail of the redshift distribution and the ELGs are expected to live in low-mass haloes, we recover a low signal-to-noise ratio around 2 for  $R < 1$  Mpc.

We model the measurement using a truncated Navarro, Frank & White halo profile (Baltz, Marshall & Oguri 2009) and the mass–concentration relation from Neto et al. (2007) to truncate haloes at half their concentration (Wright & Brainerd 2000). The best-fitting model suggests typical halo masses of  $M_{200} = 1.25 \pm 0.45 \times 10^{12} h^{-1} M_\odot$ . The lower and upper mass limits are, respec-

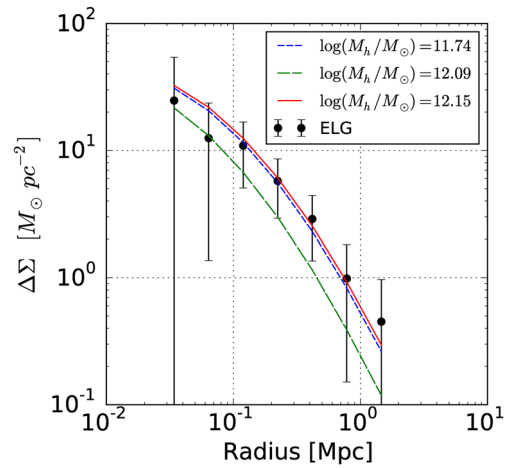


**Figure 4.** ELG surface density ( $\Delta\Sigma$ ) as a function of the physical scale for different lens models.

tively,  $M_{200} = 5.61 \pm 7.20 \times 10^{11} h^{-1} M_\odot$  and  $M_{200} = 1.41 \pm 0.51 \times 10^{12} h^{-1} M_\odot$ ; see Fig. 4. This measurement is in good agreement with the first interpretations based on the clustering (see Section 3).

## 4 HALO OCCUPATION FOR EMISSION LINE GALAXIES

The SHAM (e.g. Conroy et al. 2006; Trujillo-Gomez et al. 2011) technique is a straightforward method to link observed galaxies with dark-matter-only simulated haloes. It relies in a monotonic correspondence between halo and galaxy number densities, which is based on the assumption that more luminous galaxies reside in more massive haloes. Such association is performed by choosing suitable proxies for both haloes and galaxies (e.g. the halo maximum circular velocity and the galaxy luminosity or stellar mass) and includes some scatter [see Trujillo-Gomez et al. (2011) for details]. The advantage of using  $N$ -body simulations, compared to analytical models, is given by the accuracy achieved in the predictions of the clustering for a given halo population. Many state-of-the-art clustering measurements have been modelled using a SHAM technique that maps the observations on to suitable high-resolution  $N$ -body simulations, allowing the interpretation of the HOD and bias (de la Torre et al. 2013; Nuza et al. 2013; Carretero et al. 2015). Watson et al. (2015) recently presented a method to upgrade SHAM models to account for differences between quenched and star-forming galaxies.

In the specific case of the ELGs, the traditional SHAM approach cannot be applied since it requires a complete galaxy sample, and ELGs are far from being complete in any parameter space, even in terms of their emission line luminosity, see Comparat et al. (2013). We therefore must modify the standard SHAM procedure to take into account the ELG incompleteness and match their clustering amplitude. To this purpose, we selected haloes and subhalos by mass (for the subhalos we considered only the mass of the bound particles, to avoid ambiguities) to be able to compare directly with the weak lensing measurements. In the future, provided a high signal-to-noise ratio in the clustering measurement, we will properly select (sub)haloes by their maximum circular velocity at accretion, (e.g. Behroozi et al. 2013).

In order to model both the 1-halo and the 2-halo terms in the ELG two-point correlation functions and the weak lensing measurement,

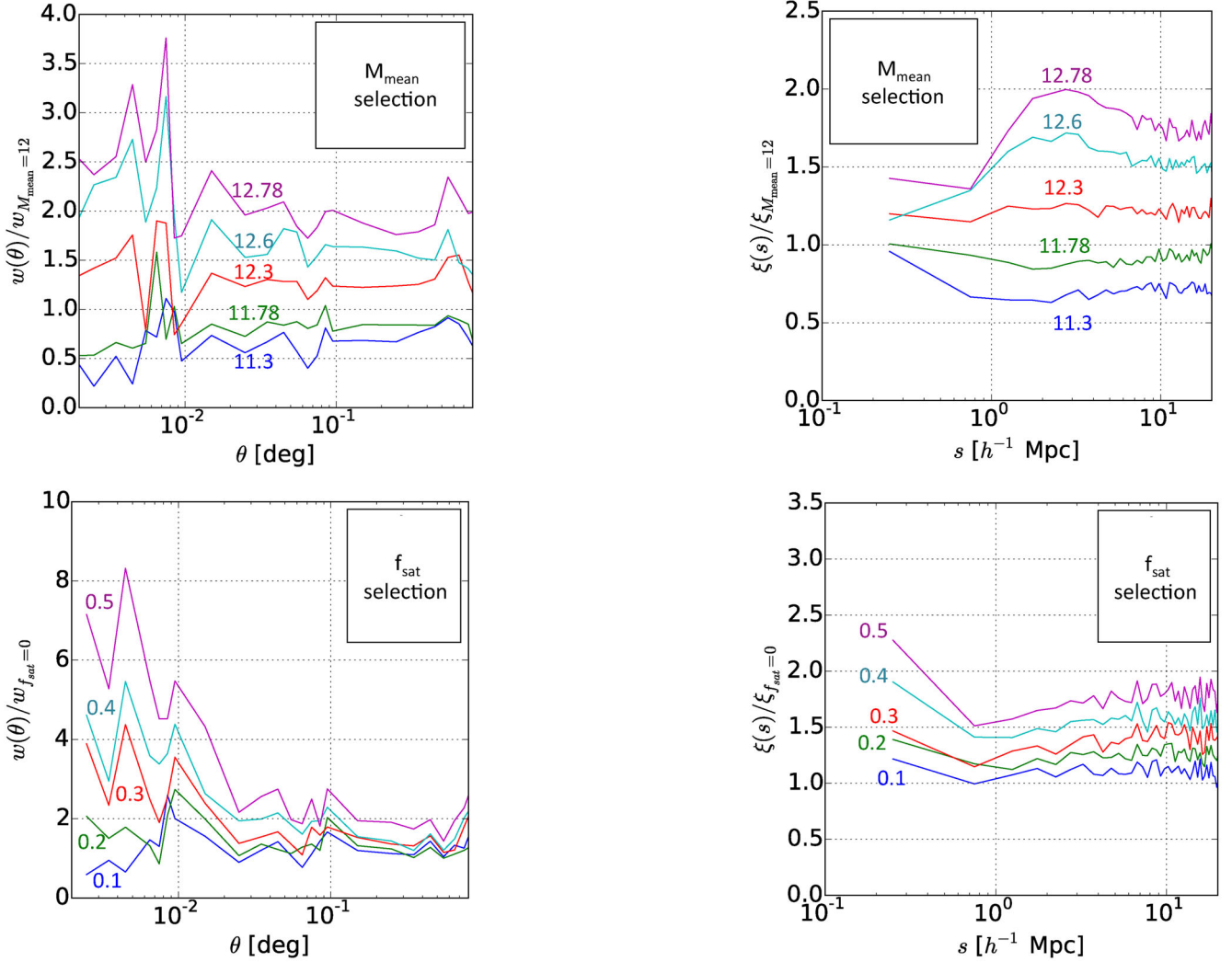


**Figure 5.** Left column, top panel: ratio of the angular correlation functions of the MDPL-LC haloes selected by mass, to  $w(\theta)$  computed at  $M_{\text{mean}} = 10^{12} h^{-1} M_{\odot}$ . The curves in the plot go from lower mass (bottom line) to higher mass (top line). Left column, bottom panel: ratio of the angular correlation functions of the MDPL-LC haloes with varying satellite fraction, to  $w(\theta)$  computed at  $f_{\text{sat}} = 0$ . The lines in the plot go from lower  $f_{\text{sat}}$  (bottom line) to higher  $f_{\text{sat}}$  (top line). Right column: same results for the monopole. The top row presents our first experiment (see the text for details) on the light-cone: we impose different halo mass thresholds to the MDPL-LC and apply a standard SHAM. The bottom row displays SHAM in the mass bin  $M_h = (1 \pm 0.5 \times 10^{12} h^{-1} M_{\odot})$  with varying satellite fractions.

we use the MultiDark Planck  $1 h^{-3} \text{ Gpc}^3$  box (see Section 2.2), which represents the best compromise between high resolution and volume, as previously described in Section 3.

We parametrize the probability of selecting a halo hosting an ELG as follows:

$$\begin{aligned}
 P(M_h, M_{\text{mean}}, \sigma_M, f_{\text{sat}}) \\
 = f_{\text{sat}} \mathcal{N}(M_h, M_{\text{mean}}, \sigma_M, \text{flag} = \text{sat}) \\
 + (1 - f_{\text{sat}}) \mathcal{N}(M_h, M_{\text{mean}}, \sigma_M, \text{flag} = \text{cen})
 \end{aligned} \quad (4)$$

where  $\mathcal{N}$  is a Gaussian distribution with the variable being  $M_h$ , the halo mass. The parameters are:  $M_{\text{mean}}$ , the mean halo mass of the sample including both host and satellite haloes;  $\sigma_M$ , the dispersion around the mean halo mass;  $f_{\text{sat}}$ , the satellite fraction. The additional parameter ‘flag’ enables to identify among the haloes the ones that are centrals (flag = cen) or the ones that are satellites (flag = sat).

To qualitatively understand the dependence of clustering on  $M_{\text{mean}}$  and  $f_{\text{sat}}$ , we impose (i) a maximum halo mass threshold to the MDPL-

LC by removing all haloes with  $M_h > M_{\text{max}}$  and we apply the standard SHAM procedure. The higher-mass ( $M_{\text{max}} > 10^{13} h^{-1} M_{\odot}$ ) models reproduce well the observed  $w(\theta)$ , and that the lower-mass models ( $M_{\text{max}} < 10^{13} h^{-1} M_{\odot}$ ) match the large-scale clustering, but not the small-scale amplitude witnessed below  $\theta \sim 0.01^\circ$ . The top row in Fig. 5 displays the ratio between the angular (left-hand panel) and the monopole (right) correlation functions of the lower-mass models and the model with  $M_{\text{mean}} = 10^{12} h^{-1} M_{\odot}$ . We see a mild variation in  $w(\theta)$  as a function of the physical scale, and a flatter trend in the monopole.

We next (ii) fix the halo mass by selecting all the haloes in the mass bin  $M_h = (1 \pm 0.5 \times 10^{12} h^{-1} M_{\odot})$ , and vary the satellite fraction. We split this halo catalogue into two catalogues, one containing only central haloes ( $f_{\text{sat}} = 0$ ) and one with satellites; then downsample both mocks to match the ELG  $n(z)$ . The bottom panels in Fig. 5 present the variation of the angular and monopole clustering as a function of the scale. At small scales the amplitude of  $w(\theta)$  with more than 30 per cent satellite fraction is strongly



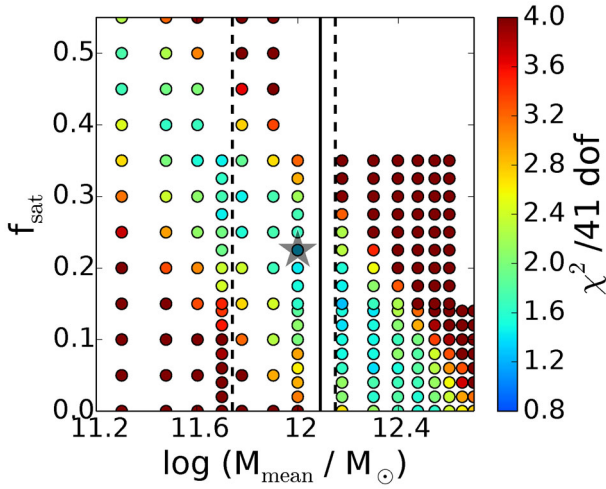


**Figure 6.** The two parameters driving the model: fraction of satellite ( $f_{\text{sat}}$ ) and mean halo mass ( $M_{\text{mean}}$ ). The spread around the mean halo mass is fixed at the value  $\sigma_M = M_{\text{mean}}/2$ . The vertical black lines represent the constraints by weak lensing (dashed: lower and upper limits; solid: mean), which rule out the majority of the low-mass and high-mass models. Our best-fitting model is highlighted by the star symbol.

enhanced compared to the 10 – 20 per cent cases. In the monopole there is almost no variation with the scale. We then combine these two products to build galaxy mock catalogues that contain a  $f_{\text{sat}}$  fraction of satellites (taken from the satellite-only mock) and  $(1-f_{\text{sat}})$  centrals (from the central-only mock). Satellite fractions between 20 per cent and 30 per cent account for the clustering signal on both small and large scales; see Fig. 6. All the selections above are done on the halo mass defined as  $M_{200}$ , which correspond to an overdensity threshold of  $\Delta_{200} = 200\rho_c$  (Prada et al. 2012), where  $\rho_c$  is the critical density of the Universe.

To produce a mock catalogue, we randomly select haloes from the light-cone according to the probability distribution  $P$ , defined in equation (4), until the ELG redshift distribution  $n(z)$  in Fig. 2 is achieved. We then construct a grid of mocks by selecting  $M_{\text{mean}}$  in the range  $10^{11.2} - 10^{12.7} h^{-1} M_\odot$ ,  $\sigma_M$  between the values  $M_{\text{mean}}/[1., 2., 4.] h^{-1} M_\odot$  (the sampling space is three times larger), and the satellite fraction in the interval  $0 < f_{\text{sat}} < 0.5$ , to obtain predictions for both  $\xi^s$  and  $w(\theta)$ . Finally, we compare these model predictions with our measurements by computing a combined  $\chi^2$  on scales  $2 < s < 22 h^{-1}$  Mpc for the monopole, and  $0.002 < \theta < 0.55$  for the angular clustering, as follows:

$$\chi^2 = \frac{N_\xi \chi_\xi^2 + N_w \chi_{w(\theta)}^2}{N_\xi + N_w}, \quad (5)$$

where

$$\chi_{w(\theta)}^2 = \frac{1}{N_w} \sum_i \frac{|w_{\text{observed}}(\theta_i) - w_{\text{haloes}}(\theta_i)|^2}{\sigma^2(w_{\text{observed}}(\theta_i))}, \quad (6)$$

and

$$\chi_\xi^2 = \frac{1}{N_\xi} \sum_i \frac{|\xi_{\text{observed}}(s_i) - \xi_{\text{haloes}}(s_i)|^2}{\sigma^2(\xi_{\text{observed}}(s_i))}. \quad (7)$$

The possible models accounting for the ELG clustering are degenerate with respect to the mean halo mass and the satellite fraction. In fact, Fig. 6 shows that a plethora of  $(\log M_{\text{mean}}, f_{\text{sat}})$  models fit the data: from  $(11.3, 0.45)$  by  $(12, 0.2)$  to  $(12.5, 0)$ . Given the 41 degrees of freedom we have, we consider acceptable those models

with  $\chi^2 < 1.25$ . Models with a higher  $\chi^2$  value are rejected at the 90 per cent level.

The combination with the weak lensing results breaks this degeneracy and rules out the higher- and lower-mass models. However, among these latter, there is one with  $\chi^2 = 1$  and parameters:  $\log M_{\text{mean}} = 12$ ,  $\sigma_M = M_{\text{mean}}/2$ ,  $f_{\text{sat}} = 22.5$  per cent (star symbol in Fig. 6). The angular and redshift-space correlation functions of this best-fitting mock are displayed in Fig. 3 (blue line), together with the ELG measurements. The weak lensing measurement are perfectly compatible with this best-fitting model.

We provide our best-fitting MDPL mock catalogue to the ELG clustering measurements at <http://projects.ift.uam-csic.es/skies-universes/>.

## 5 RESULTS AND DISCUSSION

### 5.1 ELG clustering trends as a function of magnitude, flux, luminosity and stellar mass

We employ the complete VIPERS data sample at  $z \sim 0.8$ , which has about 30 000 reliable redshifts in the range  $0.6 < z < 1$ , to investigate trends of the clustering amplitude (bias) with observed or rest frame broad-band magnitude or emission line flux. To this purpose, we measure the emission line properties in the VIPERS spectra and find a significant [O II] flux in about two thirds of them; the rest does not show emission lines (Comparat et al. 2016). We bin the data according to apparent and absolute magnitude, [O II] flux and luminosity, and measure the clustering in each sample (the binning scheme was set to contain between 9000 and 10 000 data points). Fig. 7 shows our ELG results in the observed (bottom row) and rest frame (top row). Consistently with previous analyses (e.g. Marulli et al. 2013; Mostek et al. 2013), we find that the brighter the selection in the  $i$ -band, either observed or rest frame, the higher the bias. Analogously, the fainter the  $g$ -band limit, either observed or rest frame, the higher the bias. The anti-correlation between [O II] flux and bias is only seen in the observed frame (the difference is  $\sim 1.4$ ); in the rest frame it is not significant. It would be interesting to further investigate the correlation between [O II] luminosity and  $g$ -band magnitude in the small-scale clustering, but with the resolution of current data we are not able to push the analysis to scales  $\sim 200 h^{-1}$  kpc, which is the typical virial radius of a halo of mass  $10^{12} h^{-1} M_\odot$ . New data from eBOSS will be able to address this issue. The results above indicate that if we have a  $g$ -selected ELG sample and [O II] fluxes for a certain number of its galaxies, in order to maximize its clustering signal, we should select the ELGs with brighter  $i$ -band magnitudes.

To investigate the clustering dependence on stellar mass, we map the host halo masses for ELGs at  $z \sim 0.8$ ,  $M_h \sim 10^{12} h^{-1} M_\odot$ , on to stellar mass values using the SHMR by Leauthaud et al. (2012), see their fig. 11. Our data are right before the ‘knee’ at  $M_* \sim 3.5 \times 10^{10} h^{-1} M_\odot$ .

### 5.2 Star formation efficiency

From our analysis, the typical halo masses hosting ELGs at  $z \sim 0.8$  are  $M_h \sim (1 \pm 0.5) \times 10^{12} h^{-1} M_\odot$ , and 22.5 per cent  $\pm 2.5$  per cent of them are satellites belonging to a larger halo, whose central is a quiescent galaxy. Fig. 8 provides a schematic representation of the possible ELG configurations. A total of 22.1 per cent ELGs are single satellites belonging to a parent halo with mass  $M_{hQ} \sim 2.5 \times 10^{13} h^{-1} M_\odot$ ; only in 1.3 per cent of the cases the parent halo hosts more than one satellite ELG. The maximum number of satellites,

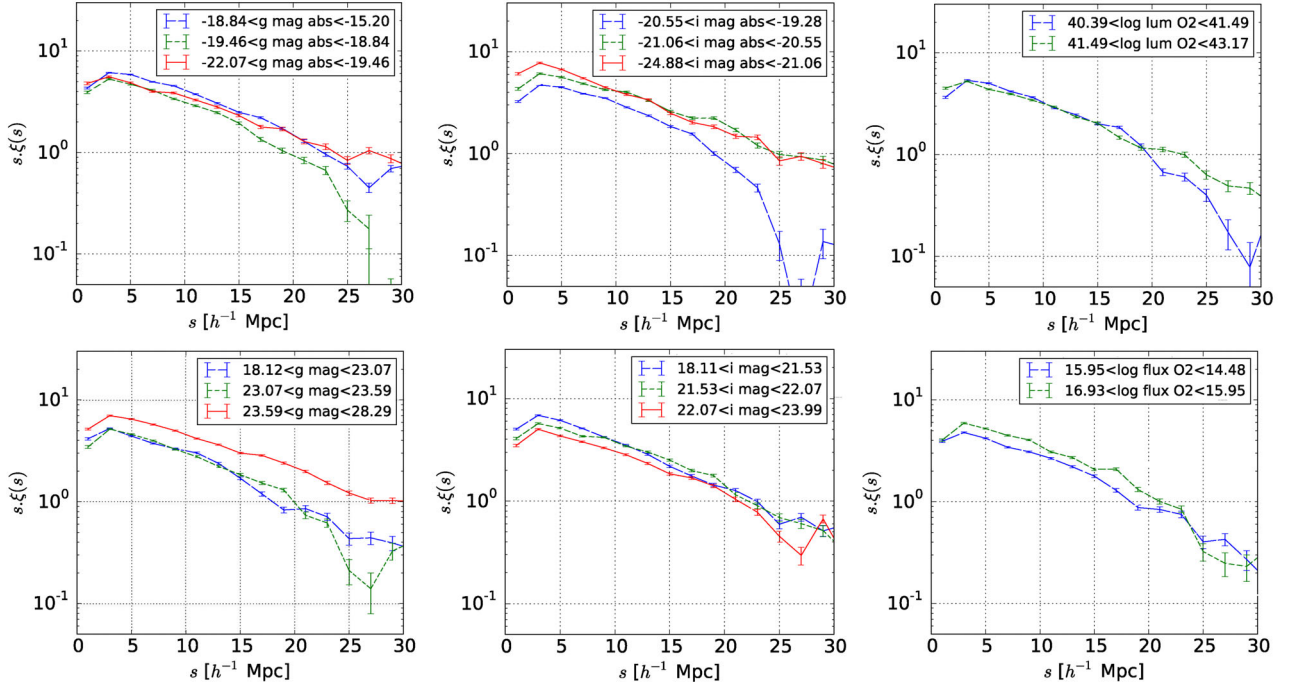


**Figure 7.** VIPERS clustering trends as a function of the  $g$ -band and  $i$ -band magnitudes (top row: rest frame; bottom row: observed frame),  $[O II]$  luminosity (top row) and  $[O II]$  flux (bottom row).

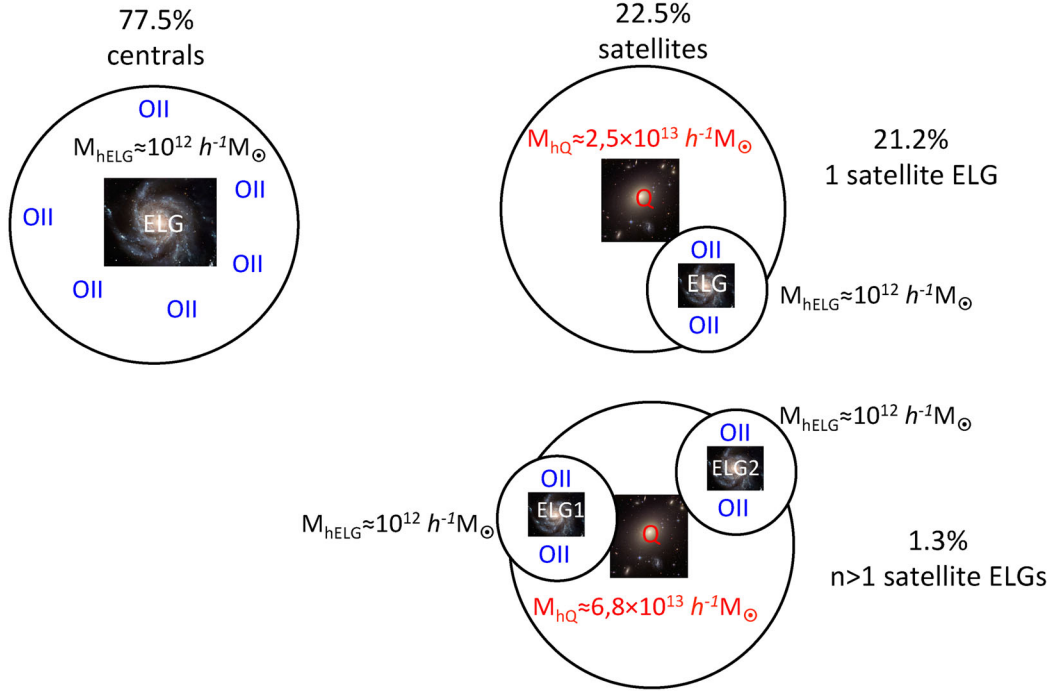


**Figure 8.** Schematic diagram of possible ELG configurations. ELGs at  $z \sim 0.8$  typically live in haloes of mass  $M_{\text{h}} \sim (1 \pm 0.5) \times 10^{12} h^{-1} M_{\odot}$  and 22.5 per cent are satellites belonging to larger haloes, whose central galaxy is quiescent. Among these satellite configurations, 21.2 per cent of parent haloes with  $M_{\text{hQ}} \sim 2.5 \times 10^{13} h^{-1} M_{\odot}$  host one satellite ELG, and only 1.3 per cent of parents host more than one satellite ELG. The maximum number of satellites,  $n = 1.8$ , is achieved in the highest-mass case,  $M_{\text{hQ}} \sim 6.8 \times 10^{13} h^{-1} M_{\odot}$ . See the text for details.

$n = 1.8$ , is achieved in the highest-mass case, where  $M_{\text{hQ}} \sim 6.8 \times 10^{13} h^{-1} M_{\odot}$ . These results imply that the mean number of ELG satellites is only slightly larger than unity ( $\sim 1.01$ ). The quiescent galaxies at the centre of the parent haloes are not included in the

sample, since the stellar masses for ELGs from the SHMR discussed above are too low for haloes of  $10^{13} h^{-1} M_{\odot}$ .

The typical masses for haloes hosting ELGs suggest that we are sampling haloes ( $\sim 10^{12} h^{-1} M_{\odot}$ ) that form stars in the most

efficient way, according to the stellar-to-halo mass ratio discussed by Behroozi, Wechsler & Conroy (2013; see their fig. 1, bottom panel). This result opens a new science field and, hopefully, in the near future, integrated models combining  $N$ -body simulations with SAMs will be able to probe star formation and shed some light on the correlations between [O II] flux and magnitude in the clustering of galaxies.

## 6 SUMMARY

We have presented an analysis of the HOD for ELGs, which jointly accounts for three measurements: the angular correlation function, the monopole, and the weak lensing signal around ELGs (see Section 3). Our procedure can be summarized in the following points:

- (i) Apply the SUGAR (Rodríguez-Torres et al. 2016) algorithm to the 11 snapshots available from the MDPL simulation to construct a light-cone (Section 2.2), with the same geometry and angular footprint of the ELG data.
- (ii) Modify the traditional SHAM technique (Section 4), to account for the ELG incompleteness, by selecting model galaxies by mass, until we match the observed ELG  $n(z)$ . In this way, our mock is constrained by the observed ELG redshift distribution, and represents a reliable model.
- (iii) Parametrize the probability of selecting a halo hosting a ELG with equation (4), in terms of the mean halo mass of the sample ( $M_{\text{mean}}$ ), the dispersion around the mean ( $\sigma_M$ ), and the satellite fraction ( $f_{\text{sat}}$ ). The additional parameter ‘flag’ enables to distinguish central and satellite haloes.
- (iv) We perform two experiments (see Section 4) on the MDPL light-cone to derive information on which are the halo mass and satellite fraction ranges of values we need to input in our modified SHAM model to correctly fit the ELG clustering signal.
- (v) Construct a grid of models based on these values, and jointly fit both angular and redshift-space clustering (see Section 4). Our best-fitting models (see Fig. 6) are degenerate with respect to  $M_{\text{mean}}$  and  $f_{\text{sat}}$ . The combination with the weak lensing analysis (see Section 3.1) breaks this degeneracy and rules out the highest and lowest mass models. Our best-fitting ( $\chi^2 = 1$ ) model is shown in Fig. 3 together with the ELG measurements, and is given by  $\log M_{\text{mean}} = 12$ ,  $f_{\text{sat}} = 22.5$  per cent,  $\sigma_M = M_{\text{mean}}/2$ .

To conclude, we have built and released to the community a reliable galaxy mock catalogue that correctly fits the clustering amplitude of the *ugri* ELG sample constructed by matching spectroscopic redshifts from BOSS DR12, VIPERS and DEEP2 (for details see Section 2). With these tools, we can begin building many realizations of the density field to predict errors on the BAO measurement.

The measured halo masses for haloes hosting ELGs indicate that we are sampling the haloes that form stars in the most efficient way, according the stellar-to-halo mass ratio discussed by Behroozi et al. (2013; see their fig. 1, bottom panel). This is an important point for the future, and opens the path to further studies to understand the correlation between clustering and the strength of emission lines. With the resolution available from current data, we are not able to push the analysis to the typical scales ( $\sim 200 h^{-1}$  kpc) of haloes of  $10^{12} h^{-1} M_{\odot}$ ; however, next-generation surveys, as eBOSS and DESI, will provide better resolution, and in the near future we should be able to build robust combinations of  $N$ -body simulations and SAMs that will address those questions.

## ACKNOWLEDGEMENTS

GF is supported by the Ministerio de Educación y Ciencia of the Spanish Government through FPI grant AYA2010-2131-C02-01. JC acknowledges financial support from MINECO (Spain) under project number AYA2012-31101. GY acknowledges financial support from MINECO (Spain) under project number AYA2012-31101 and grant FPA2012-34694. EJ acknowledges the support of CNRS, and the Labex OCEVU. SEN acknowledges support by the Deutsche Forschungsgemeinschaft under the grant NU 332/2-1. GF, FP, SART, AK, SN and CC acknowledge financial support from the Spanish MICINN Consolider-Ingenio 2010 Programme under grant MultiDark CSD2009-00064, MINECO Centro de Excelencia Severo Ochoa Programme under grant SEV-2012-0249, and MINECO grant AYA2014-60641-C2-1-P. GF, JC and FP wish to thank the Lawrence Berkeley National Laboratory for the hospitality during the creation of this work. FP acknowledges the spanish MEC ‘Salvador de Madariaga’ program, Ref. PRX14/00444.

The MultiDark Planck simulation has been performed in the Supermuc supercomputer at the Libniz Supercomputing Center (LRZ, Munich) thanks to the cpu time awarded by PRACE (proposal number 2012060963).

Funding for SDSS-III has been provided by the Alfred P. Sloan Foundation, the Participating Institutions, the National Science Foundation, and the US Department of Energy Office of Science. The SDSS-III web site is <http://www.sdss3.org/>.

SDSS-III is managed by the Astrophysical Research Consortium for the Participating Institutions of the SDSS-III Collaboration including the University of Arizona, the Brazilian Participation Group, Brookhaven National Laboratory, Carnegie Mellon University, University of Florida, the French Participation Group, the German Participation Group, Harvard University, the Instituto de Astrofísica de Canarias, the Michigan State/Notre Dame/JINA Participation Group, Johns Hopkins University, Lawrence Berkeley National Laboratory, Max Planck Institute for Astrophysics, Max Planck Institute for Extraterrestrial Physics, New Mexico State University, New York University, Ohio State University, Pennsylvania State University, University of Portsmouth, Princeton University, the Spanish Participation Group, University of Tokyo, University of Utah, Vanderbilt University, University of Virginia, University of Washington, and Yale University.

## REFERENCES

- Abazajian K. N. et al., 2009, *ApJS*, 182, 543
- Alam S. et al., 2015, *ApJS*, 219, 12
- Anderson L. et al., 2014, *MNRAS*, 441, 24
- Baldry I. K., Glazebrook K., Brinkmann J., Ivezić Ž., Lupton R. H., Nichol R. C., Szalay A. S., 2004, *ApJ*, 600, 681
- Baltz E. A., Marshall P., Oguri M., 2009, *J. Cosmol. Astropart. Phys.*, 1, 15
- Bartelmann M., 1999, in Banday A. J., Sheth R. K., da Costa L. N., eds, *Evolution of Large Scale Structure: From Recombination to Garching*. European Southern Observatory, Garching, p. 213
- Behroozi P. S., Wechsler R. H., Conroy C., 2013, *ApJ*, 762, L31
- Behroozi P. S., Wechsler R. H., Wu H.-Y., Busha M. T., Klypin A. A., Primack J. R., 2013, *ApJ*, 763, 18
- Berlind A. A., Weinberg D. H., 2002, *ApJ*, 575, 587
- Blaizot J., Wadadekar Y., Guiderdoni B., Colombi S. T., Bertin E., Bouchet F. R., Devriendt J. E. G., Hatton S., 2005, *MNRAS*, 360, 159
- Blanton M. R., Lin H., Lupton R. H., Maley F. M., Young N., Zehavi I., Loveday J., 2003, *AJ*, 125, 2276
- Bolton A. S. et al., 2012, *AJ*, 144, 144
- Bray A. D. et al., 2015, *ApJ*, 811, 90

- Carretero J., Castander F. J., Gaztañaga E., Crocce M., Fosalba P., 2015, *MNRAS*, 447, 646
- Coil A. L. et al., 2008, *ApJ*, 672, 153
- Comparat J. et al., 2013, *MNRAS*, 433, 1146
- Comparat J. et al., 2015, *A&A*, 575, A40
- Comparat J. et al., 2016, preprint ([arXiv:1605.02875](https://arxiv.org/abs/1605.02875))
- Conroy C., Wechsler R. H., Kravtsov A. V., 2006, *ApJ*, 647, 201
- Cooper M. C. et al., 2008, *MNRAS*, 383, 1058
- Cooray A., Sheth R., 2002, *Phys. Rep.*, 372, 1
- Coupon J. et al., 2009, *A&A*, 500, 981
- Coupon J. et al., 2012, *A&A*, 542, A5
- Coupon J. et al., 2015, *MNRAS*, 449, 1352
- Dawson K. S. et al., 2013, *AJ*, 145, 10
- Dawson K. S. et al., 2016, *AJ*, 151, 44
- de la Torre S. et al., 2013, *A&A*, 557, A54
- Eisenstein D. J. et al., 2011, *AJ*, 142, 72
- Erben T. et al., 2013, *MNRAS*, 433, 2545
- Favole G., McBride C. K., Eisenstein D. J., Prada F., Swanson M. E., Chuang C.-H., Schneider D. P., 2015, preprint ([arXiv:1506.02044](https://arxiv.org/abs/1506.02044))
- Fukugita M., Ichikawa T., Gunn J. E., Doi M., Shimasaku K., Schneider D. P., 1996, *AJ*, 111, 1748
- Garilli B. et al., 2014, *A&A*, 562, A23
- Gillis B. R. et al., 2013, *MNRAS*, 431, 1439
- Gunn J. E. et al., 2006, *AJ*, 131, 2332
- Guo H. et al., 2014, *MNRAS*, 441, 2398
- Guo H. et al., 2015, *MNRAS*, 453, 4368
- Guzzo L. et al., 2014, *A&A*, 566, A108
- Hearin A. P., Watson D. F., 2013, *MNRAS*, 435, 1313
- Hearin A. P., Watson D. F., Becker M. R., Reyes R., Berlind A. A., Zentner A. R., 2014, *MNRAS*, 444, 729
- Heymans C. et al., 2012, *MNRAS*, 427, 146
- Ilbert O. et al., 2006, *A&A*, 457, 841
- Kitzbichler M. G., White S. D. M., 2007, *MNRAS*, 376, 2
- Klypin A., Holtzman J., 1997, preprint ([arXiv:astro-ph/9712217](https://arxiv.org/abs/astro-ph/9712217))
- Klypin A., Prada F., Yepes G., Hess S., Gottlöber S., 2013, preprint ([arXiv:1310.3740](https://arxiv.org/abs/1310.3740))
- Klypin A., Yepes G., Gottlöber S., Prada F., Hess S., 2014, preprint ([arXiv:1411.4001](https://arxiv.org/abs/1411.4001))
- Kravtsov A. V., Berlind A. A., Wechsler R. H., Klypin A. A., Gottlöber S., Allgood B., Primack J. R., 2004, *ApJ*, 609, 35
- Landy S. D., Szalay A. S., 1993, *ApJ*, 412, 64
- Laureijs R. et al., 2011, preprint ([arXiv:1110.3193](https://arxiv.org/abs/1110.3193))
- Leauthaud A., Tinker J., Behroozi P. S., Busha M. T., Wechsler R. H., 2011, *ApJ*, 738, 45
- Leauthaud A. et al., 2012, *ApJ*, 744, 159
- Marulli F. et al., 2013, *A&A*, 557, A17
- Mostek N., Coil A. L., Cooper M., Davis M., Newman J. A., Weiner B. J., 2013, *ApJ*, 767, 89
- Neto A. F. et al., 2007, *MNRAS*, 381, 1450
- Newman J. A. et al., 2013, *ApJS*, 208, 5
- Nuza S. E. et al., 2013, *MNRAS*, 432, 743
- Oke J. B., Gunn J. E., 1983, *ApJ*, 266, 713
- Planck Collaboration XVI, 2014, *A&A*, 571, A16
- Prada F., Klypin A. A., Cuesta A. J., Betancort-Rijo J. E., Primack J., 2012, *MNRAS*, 423, 3018
- Reid B. A., Seo H.-J., Leauthaud A., Tinker J. L., White M., 2014, *MNRAS*, 444, 476
- Riebe K. et al., 2013, *Astron. Nachr.*, 334, 691
- Rodríguez-Torres S. A. et al., 2016, *MNRAS*, 460, 2
- Sartoris B. et al., 2016, *MNRAS*, 459, 1764
- Schlegel D. J. et al., 2015, *Am. Astron. Soc. Meeting Abstr.*, Vol. 225
- Scoville N. et al., 2007, *ApJS*, 172, 150
- Shan H. et al., 2015, preprint ([arXiv:1502.00313](https://arxiv.org/abs/1502.00313))
- Skibba R. A. et al., 2015, *ApJ*, 807, 152
- Smee S. A. et al., 2013, *AJ*, 146, 32
- Smee S. A. et al., 2014, *Proc. SPIE*, 9147, 91472V
- Stoughton C. et al., 2002, *AJ*, 123, 485
- Sugai H. et al., 2012, *Proc. SPIE*, 8446, 84460Y
- Swanson M. E. C., Tegmark M., Blanton M., Zehavi I., 2008, *MNRAS*, 385, 1635
- Tinker J. L., Robertson B. E., Kravtsov A. V., Klypin A., Warren M. S., Yepes G., Gottlöber S., 2010, *ApJ*, 724, 878
- Trujillo-Gomez S., Klypin A., Primack J., Romanowsky A. J., 2011, *ApJ*, 742, 16
- Velander M., Kuijken K., Schrabback T., 2011, *MNRAS*, 412, 2665
- Wang Y., Yang X., Mo H. J., van den Bosch F. C., 2007, *ApJ*, 664, 608
- Watson D. F. et al., 2015, *MNRAS*, 446, 651
- Weinberg D. H., Mortonson M. J., Eisenstein D. J., Hirata C., Riess A. G., Rozo E., 2013, *Phys. Rep.*, 530, 87
- Wright C. O., Brainerd T. G., 2000, *ApJ*, 534, 34
- York D. G. et al., 2000, *AJ*, 120, 1579
- Zehavi I. et al., 2005, *ApJ*, 630, 1
- Zehavi I. et al., 2011, *ApJ*, 736, 59
- Zheng Z. et al., 2005, *ApJ*, 633, 791
- Zheng Z., Coil A. L., Zehavi I., 2007, *ApJ*, 667, 760

This paper has been typeset from a  $\text{\LaTeX}$  file prepared by the author.